

Interpretable Retinal Disease Prediction Using Biology-Informed Heterogeneous Graph Representations

Laurin Lux  *laurin.lux@tum.de*, Alexander H. Berger, Maria Romeo Tricas, Richard Rosen, Alaa E. Fayed, Sobha Sivaprasada, Linus Kreitner, Jonas Weidner, Martin J. Menten, Daniel Rueckert and Johannes C. Paetzold

Munich Center for Machine Learning (MCML), Munich, Germany

School of Medicine and Health, TUM University Hospital, Munich, Germany

School of Computation, Information and Technology, TUM, Munich, Germany

Weill Cornell Medicine, Cornell University, New York City, , New York, USA

Abstract

Interpretability is crucial for utilizing machine learning models as clinical decision support tools for medical diagnostics. However, most state-of-the-art image classifiers based on neural networks are not interpretable. As a result, clinicians often resort to known biomarkers to guide diagnosis, although biomarker-based classification often suffers from drastic information loss compared to raw medical images. This work proposes a method that preserves the rich imaging information while simultaneously enhancing the interpretability of predictions for diabetic retinopathy staging from optical coherence tomography angiography (OCTA) images. Our method is based on a novel biology-informed heterogeneous graph representation that models retinal vessel segments, intercapillary areas, and the foveal avascular zone (FAZ) in a human-interpretable way. This graph representation allows us to frame diabetic retinopathy (DR) staging as a graph-level classification task, which we solve using an efficient graph neural network. We compare our method against established methods, including classical biomarker-based classifiers, convolutional neural networks (CNNs), and vision transformers in predicting the clinically assigned DR stage based on color fundus photogra-

phy images. We find stage agreement rates of our method and alternative vision model based classifiers saturating at AUC-ROC values of 84%. Crucially, we use our biology-informed graph to provide explanations of unprecedented detail. Our approach surpasses existing methods in precisely localizing and identifying abnormal vessels and non-perfusion areas. Our approach sets the stage for the interpretable identification of patients who require special attention due to their traceable microvascular changes, only observable using the details of OCTA images.

1. Introduction

Diabetic Retinopathy (DR), a complication of diabetes that affects the retinal vasculature, is one of the leading causes of blindness in adulthood [1]. It is associated with pathological changes to the retinal microvasculature, such as loss of capillaries through capillary degeneration, the occurrence of intraretinal microvascular abnormalities, microaneurysms, and also neovascularization.

Optical coherence tomography angiography (OCTA), a non-invasive and high-resolution retinal imaging technique [2, 3], has emerged as a powerful tool for studying these microvascular changes. OCTA enables detailed examination of the retinal vasculature [4] down to the capillary level by resolving the superficial vascular complex (SVC) and deep vascular complex (DVC), facilitating early-stage DR detection [5].

Currently, clinicians study quantitative biomarkers extracted from OCTA images to characterize DR-related microvascular alterations, including vessel density, vessel tortuosity, and foveal avascular zone (FAZ) area. However, these biomarkers have important limitations: they fail to fully capture complex pathological changes such as intraretinal microvascular abnormalities and neovascularization, and simple metrics like tortuosity index and vessel density lack spatial localization, making clinical verification challenging. Deep learning models, that are already well-established for other imaging modalities [6], offer the potential to extract the full spectrum of microvascular pathological information from OCTA images to guide clinical diagnosis beyond traditional biomarkers. Such AI-based OCTA analysis could serve as a valuable support tool within the multimodal diagnostic workflow that integrates OCT, color fundus photography, fluorescein angiography, and patient history.

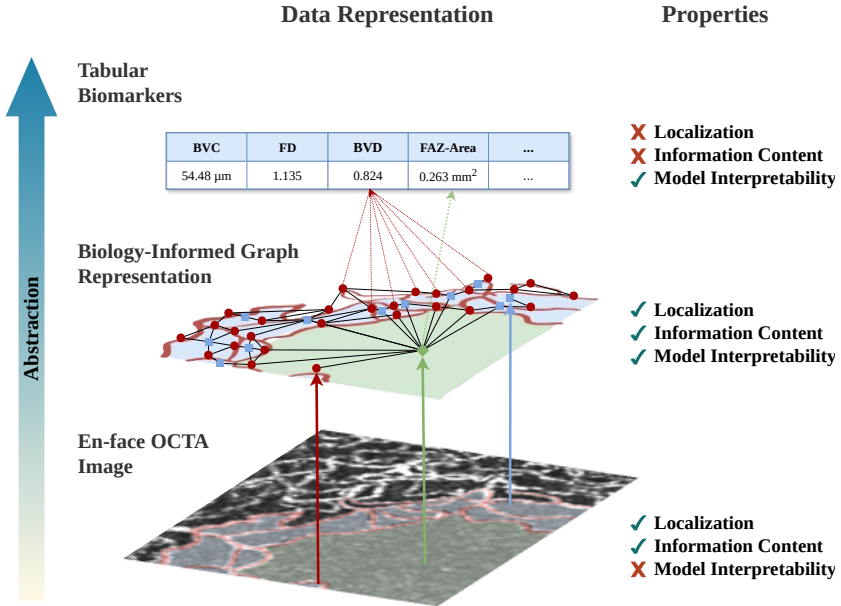


Figure 1: Schematic illustration of our heterogeneous graph representing the retinal vasculature. We elevate the image to a higher abstraction level, where nodes represent understandable biological concepts, such as vessels, intercapillary areas, and the FAZ. Because of each node’s biological meaning, known tabular biomarkers are naturally encoded in our heterogeneous graph. Consequently, classifiers trained on our representation combine the favorable interpretability of tabular biomarkers with image-level localization and performance.

Current Machine Learning (ML)-based approaches trained on OCTA images and OCTA-extracted biomarkers have shown good performance for diagnosing DR [3, 7, 8, 9, 10, 11, 12]. However, these deep learning (DL) approaches are not used for clinical decision-making, partially because their black-box predictions cannot be effectively combined with the multi-modal information sources that ophthalmologists routinely use for DR assessment. Specifically, the lack of interpretability makes it difficult for clinicians to understand how OCTA-based predictions relate to findings from other imaging modalities and patient factors, hindering their integration into comprehensive diagnostic evaluations. Although DL models may implicitly leverage high-level pathological concepts (e.g., non-perfusion areas or microaneurysms), existing explainability methods fail to attribute the model’s decisions to these concepts. For convolutional neural networks (CNNs), CAM [13] and grad-CAM [14] are common methods that focus on localizing critical image re-

gions. Previous studies [10, 11, 12] employed these explainability methods for DR classification, yielding mixed results. While their approaches allowed a rough identification of critical image regions, the emphasized areas remain broad and unspecific. Moreover, the most critical shortcoming of these methods is the semantic gap between the highlighted image regions and human-interpretable concepts. Unlike DL approaches, inherently interpretable models, such as simple decision trees based on human-understandable biomarkers, do not achieve state-of-the-art prediction accuracy.

To address the challenge of interpretable OCTA image analysis with DL, we introduce a novel graph representation for OCTA images, combined with a methodological framework, for accurate and interpretable DR staging.¹ Specifically, our contributions are as follows:

1. We introduce a heterogeneous graph representation that expresses the biological structures in OCTA images. It preserves spatial and semantic information content while abstracting from the raw image representation to make it interpretable by clinicians. Furthermore, this heterogeneous graph representation preserves neighborhood information by incorporating both homogeneous and heterogeneous edges. Figure 1 illustrates how our approach combines the raw image’s precise spatial information with the interpretative power of high-level biomarkers. The proposed representation is a foundation for diverse classification or correlation tasks, utilizing convolutional architectures such as graph neural networks (GNNs).
2. We employ a graph learning architecture to our new representation for DR staging that allows us to directly link stage predictions to clinically well-studied indicators of DR, such as abnormal vessel segments, microaneurysms, and retinal areas with decreased capillary density. With this application, we highlight the potential of our graph-based representation for further downstream tasks.
3. Finally, we utilize our interpretable model explanations combined with OCTA expert readings to identify a subgroup of patients where microvascular pathologies observed in 3 mm x 3 mm OCTA images deviate from the clinical DR stage based on color fundus images. This enables the identification of patients who require special attention for follow-up and treatment decisions.

¹Code available at <https://github.com/luxtu/OCTA-graph>.

By providing an interpretable data representation combined with an explainable and high-performing prediction algorithm, we aim to advance support tools for clinical decision-making.

2. Related Work

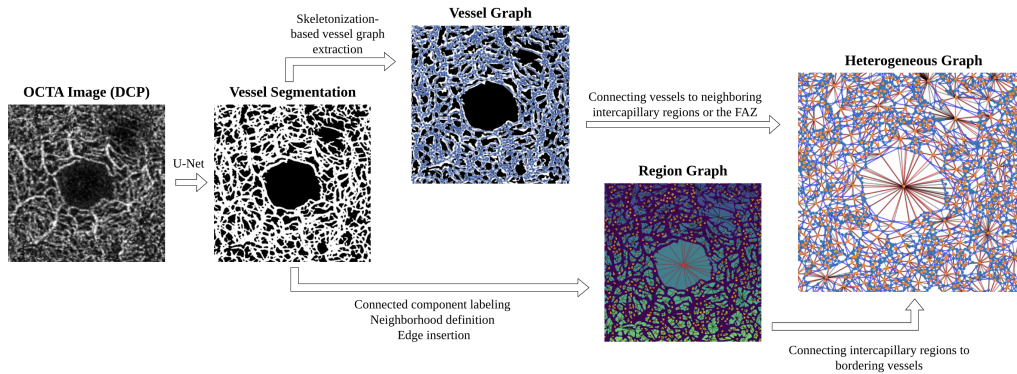


Figure 2: Processing pipeline for generating a heterogeneous graph that models an OCTA image’s most relevant biological concepts: vessels, intercapillary areas, and the FAZ. A vasculature segmentation [15] is used to create a vessel graph and intercapillary area graph and identify the FAZ. Finally, these components are merged into a single interconnected heterogeneous graph representation.

2.1. Machine Learning for DR Staging in OCTA

In recent years, the improvement of instrumentation [16] has made OCTA available to an increasing number of ophthalmologists. Since then, many studies have investigated DR with OCTA. Approaches to staging DR with OCTA can be broadly categorized into two groups. The first group comprises feature-based methods, which are based on prior knowledge of indicative biomarkers, the quantitative assessment of these markers, and decision-making based on the extracted information [3, 7, 8, 9]. Traditionally utilized biomarkers include blood vessel density (BVD), blood vessel caliber (BVC), blood vessel tortuosity, vessel perimeter index, vessel complexity index, FAZ area, and FAZ contour irregularity. These biomarkers serve as inputs for classification models such as neural networks, support vector machines (SVM), or tree-based methods such as random forests (RF). Despite their widespread acceptance and proven significance for DR disease staging, feature-based approaches have limitations. They can only rely on a priori defined biomarkers,

established based on human expertise and laborious verification procedures. To date, no existing biomarker quantifies the severity of intraretinal microvascular abnormalities as well as the severity of microaneurysms in OCTA images. Moreover, in the classification setting, existing biomarkers are usually evaluated as global metrics without localization information.

The second group comprises DL models directly operating on the raw OCTA images. Previous studies adopted well-established CNN architectures such as ResNet [17], VGG [18], and EfficientNet [19] for DR staging and achieved high accuracy. Zhou et al. proposed a transformer-based foundation model for retinal images [20], which outperformed other state-of-the-art approaches for DR staging on color fundus images. Although the network was not directly trained on OCTA images, the model has a detailed understanding of abstract retinal concepts by training on a large amount of data. DL-based methods have shown favorable performance compared to the aforementioned traditional approaches. This performance gap indicates that DL methods can extract information that, to date, has not been formalized as an established, known biomarker, such as the severity and frequency of intraretinal microvascular abnormalities. They can be combined with explainability tools, such as CAM [13] and grad-CAM [14], to highlight critical image regions [10, 11, 12]. However, the human-in-the-loop cannot overcome the semantic gap between highlighted image regions and their corresponding intensity values and the abstract concepts established later in the CNN network. Clinicians cannot verify and interpret the algorithmic outcomes beyond the localization of influential regions. Moreover, the biomarkers utilized by the CNN networks cannot be identified and formalized.

2.2. Graph Neural Networks as Explainable Models

With the advent of graph neural networks (GNNs), convolutions were generalized towards graph-structured data; oftentimes including the concept of message-passing [21, 22, 23]. This has led to the widespread application of GNNs across diverse fields, including chemistry, physics, medicine, and social sciences, where graph-structured data is abundant [24]. In biomedical image analysis, successful applications of GNNs to discriminative tasks include brain disorder classification from functional magnetic resonance images [25], multiple sclerosis disease activity prediction from MR images [26], vessel hierarchy classification in microscopic images [27], and pathology image classification [28].

In tandem with the evolution and utilization of GNN architectures, the methods for explaining their predictions have advanced. For example, gradient-based approaches, proven successful in computer vision and CNNs, effectively provided explanations for graph-based molecular property prediction [29]. Specific perturbation-based techniques tailored for graph-structured data, such as GNNExplainer [30], have been developed. Notably, GraphLime [31], drawing inspiration from LIME [32], stands out as a surrogate-based explainability method that uses local perturbations. For a comprehensive overview of other gradient-, perturbation-, or surrogate-based explanation approaches, refer to [33]. Agarwal et al. [34] analyzed various explanation methods tailored for graph classification tasks. Their study showed that integrated gradients is the most faithful and accurate explanation method, particularly on real-world datasets with known ground truth explanations.

3. Methods

3.1. Construction of a Heterogeneous Graph Representation

We establish a heterogeneous graph representation for OCTA images incorporating biological domain knowledge. This representation models biological elements found in retinal images, specifically vessel segments, intercapillary areas, and the FAZ. Moreover, we preserve neighborhood information through edge connections, which are subsequently leveraged by graph convolutional algorithms. The process of constructing the heterogeneous graph is depicted in Figure 2. Figure 3 provides a detailed illustration of the graph’s edges and nodes.

3.1.1. Vessel Segmentation

We generate vessel segmentation maps using the method by Kreitner et al. [15, 35]. This method leverages synthetic training data to create high-fidelity label maps of the retinal vasculature. The resulting label maps include even the smallest capillary vessels and are highly continuous, which is important to generate continuous vessel and intercapillary area graphs.

3.1.2. Vessel Graph

Our representation incorporates vessel graphs [36, 37] to model the vasculature in imaged eyes. Biomarkers such as vessel complexity and diameter are also encapsulated in our vessel graphs. Each vessel segment between two bifurcation points is designated as a node, and edges between vessel

nodes are established using bifurcation points. The vasculature segmentation serves as input for a graph extraction algorithm [38], which extracts the vessel graph and provides feature descriptors detailing properties such as volume, length, curvature, and surface-distance-based values for the centerline. These features serve as embeddings for the nodes in the vessel graph. For detailed descriptions of the extracted geometric features, refer to [38] and our GitHub repository. Figure 3 depicts the vessel segments as nodes v_{ves} and the edges between adjacent vessel segments as e_{ves} . We use the open-source Voreen framework, built to visualize and explore scientific data to run the graph extraction algorithm [39].

3.1.3. Intercapillary Area Graph

Intercapillary areas are indicators for disease progression in DR [40, 41]. Essentially, they are the counterparts of segmented vessels in OCTA images. We create the nodes of the intercapillary area graph using connected component labeling of the inverted segmentation map. The nodes of the intercapillary area graph are enriched with geometric descriptors such as total area, perimeter length, and eccentricity. We rely on the skeleton of the vessel segmentation to establish the edges in the intercapillary area graph. In the skeletonized segmentation map, we find edge candidates by traversing all skeleton pixels and checking if directly adjacent pixels are part of separate background components of the skeletonized segmentation map. Using the injective map of background components in the segmentation map to background components in the skeletonized segmentation map, edges are then introduced between the intercapillary areas. In Figure 3, the intercapillary area nodes v_{ICA} represent the green areas (blue nodes), and neighborhood information is encoded in the e_{ICA} edge type.

3.1.4. Foveal avascular zone

Because of its significance as a biomarker [42, 43], we assign a separate node type and unique edge types to the FAZ. The FAZ is identified as the central intercapillary area of the connected component labeling. Our used datasets are FAZ-centered during preprocessing; note that this is a necessary prerequisite for correctly identifying the FAZ. The separate node type for the FAZ adds an inductive bias for downstream algorithms. The FAZ is represented through the node v_{FAZ} (see Figure 3).

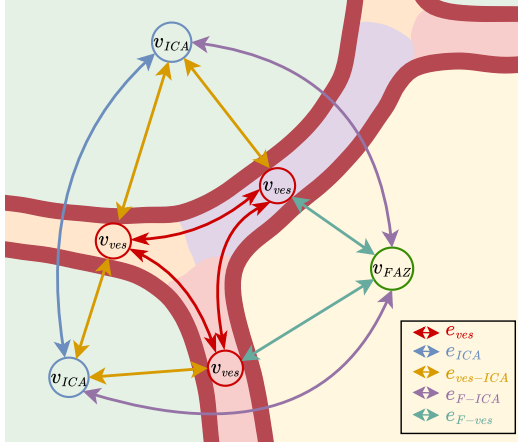


Figure 3: Schematic illustration of our heterogenous graph representation of an OCTA image. Raw pixels in the image are abstracted into either a vessel node (v_{ves}), an intercapillary area node (v_{ICA}), or the FAZ (v_{FAZ}). Neighborhood information is preserved in the homogeneous (e_{ves} , e_{ICA}) and heterogeneous edges ($e_{ves-ICA}$, e_{F-ICA} , e_{F-ves}). Interpretable geometric descriptors and intensity statistics are encoded in the node embeddings.

3.1.5. Heterogeneous Edges

In addition to the diverse node types, our representation includes heterogeneous edge connections between nodes of different types. Edges link intercapillary areas and vessels ($e_{ves-ICA}$) if an edge forms part of the border of an intercapillary area. For the FAZ, edges connect to vessels along its border (e_{F-ves}). Edges from the FAZ to intercapillary areas are created when a single vessel acts as a bisector to an intercapillary area (e_{F-ICA}).

Collectively, this biology-inspired graph representation introduces bias for downstream tasks while enhancing human interpretability by abstracting from gray values to intuitive concepts like vessels. Additionally, the graph representation preserves spatial information through superpixels in the image and neighborhood information through edges. Positional coordinates can be embedded via x- and y-coordinates for intercapillary areas and FAZ, as well as x- and y-coordinates for the start and endpoints of vessel segments. Our graph representation can be used as a foundation for various prominent prediction tasks on OCTA images (see Section 3.2 and 6).

3.2. Graph Learning for DR Staging

We utilize our heterogeneous graph representation to predict the DR stage of the imaged eye, which we frame as a graph classification task. We use the

Pytorch Geometric framework to implement our GNN model [44]. Specifically, we use a GNN architecture, as depicted in Fig. 4, tailored to our presented heterogeneous graph structure:

1. First, we preprocess the different node types separately using a block of fully connected layers for each type. Each layer is followed by a batch normalization layer for regularization and a ReLU activation function, as shown in Fig. 4 (1). These preprocessing layers can adjust the node embeddings for the following message-passing layer.
2. In the next step, we refine the embeddings based on neighborhood information using a block of independent message passing layers [23] for each edge type, see Fig 4 (2). The update using one specific type of neighborhood node, e.g., type a is then defined as

$$h_{\mathcal{N}_a(v)}^k \leftarrow \text{AGG}_{\cdot k}(\{h_u^{k-1}, \forall u \in \mathcal{N}_a(v)\}) \quad (1)$$

$$h_{v_a}^k \leftarrow \sigma(W^k \cdot (h_v^{k-1}, h_{\mathcal{N}_a(v)}^k)). \quad (2)$$

All edges are bidirectional and allow message passing in both directions. This message-passing layer is used to refine the node embeddings based on the neighborhood information stored in the graph. Using heterogeneous edges, node embeddings can be refined using the information of all types of connected neighbors. The resulting embeddings from the refinement using distinct types of neighborhood nodes are then aggregated

$$h_v^k \leftarrow \text{AGG}_{\cdot k}(\{h_{v_a}^k, h_{v_b}^k, \dots, h_{v_z}^k\}). \quad (3)$$

3. After the graph layers, another block of fully connected layers post-processes the individual representations of the different node types, see Fig 4 (3). Again, batch norm layers and a ReLU activation function are applied following each layer.
4. Next, global pooling is applied to aggregate over the embeddings of all nodes of the same type. All the aggregated embeddings of the different node types, see Fig 4 are then again aggregated into a single feature vector. (4).
5. Finally, we use an MLP head consisting of fully connected layers with dropout on the aggregated fixed-size feature vector for multiclass classification, see Fig 4 (5).

Our proposed network is restricted in its complexity compared to current CNNs and transformer models. Table 1 shows a comparison of the number

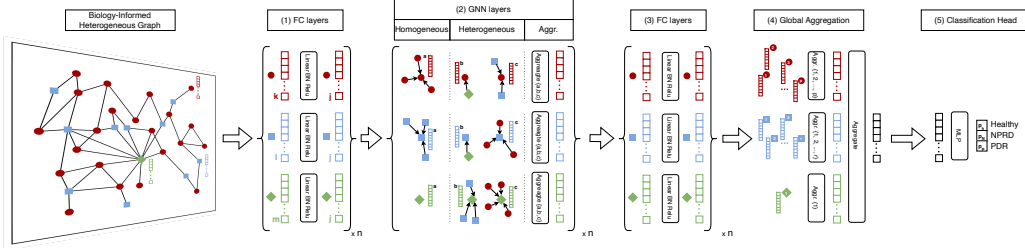


Figure 4: Illustration of the graph neural network architecture designed for the DR disease staging task. The architecture takes a heterogeneous graph as input and predicts the disease stage for the provided input graph. We generalize homogeneous message-passing architectures to the heterogeneous case by learning individual message-passing functions for each node type. After the message passing layers and linear layers, an aggregation for each node type is performed. Finally, the embeddings for all node types are aggregated and passed on to a classification head.

of parameters and the training time of the GNN model and other prominent network architectures. Notably, the graph construction step is a prerequisite for our approach. We observe that with non-runtime-optimized code, the construction takes multiple seconds. Therefore, the benefit of faster training during hyperparameter tuning outweighs the construction overhead.

3.3. Interpretability Framework for Retinal Graphs

Our explainability framework consists of two components. First, an attribution method, and second, a localization method.

3.3.1. Attribution Method

We utilize integrated gradients [45, 46] as attribution method to describe the impact of specific nodes and their characteristics on the algorithmic outcome, following the evaluations by Agarwal et al. [34]. Alternatively, the explanations can be easily adjusted to any desired attribution method. The integrated gradients approach follows a straight line path in the input feature space from a baseline sample to the target sample. In computer vision, this baseline sample is typically a zero-image. Equivalent to baseline images, graph-based approaches require a baseline vector for each node in the graph. The attribution score a_{v_i} of a feature i of a node v given a baseline x_{bl} is then defined as

$$a_{v_i} := (x_{v_i} - x_i^{bl}) \times \int_{\alpha=0}^1 \frac{\partial F(x^{bl} + \alpha \times (x - x^{bl}))}{\partial x_{v_i}} d\alpha. \quad (4)$$

Table 1: Comparison of model complexities and training times for 100 epochs with a fixed batch size of 16 on a single NVIDIA RTX A6000. The heterogeneous GNN is more than 100 times smaller than the smallest evaluated CNN model. The * indicates that the model is fine-tuned without adapting all learnable weights. Pretraining of the RetFound model required around two weeks with eight NVIDIA Tesla A100 [20].

Architecture	Data Representation	Model	Model Parameters	Train Time
CNN	Image	VGG11	133 Mio.	13 min
		ResNet18	12 Mio.	9 min
		EfficientNet B0	5 Mio.	9 min
		ConvNeXt s	50 Mio.	27 min
		ResNet50	25 Mio.	9 min
		EfficientNet V2 s	21 Mio.	11 min
Transformer	Image	RetFound Swin t	87 Mio. 28 Mio	*40 min 35 min
Heterogeneous GNN	Graph	Ours	0.04 Mio.	2 min

Instead of using a constant baseline sample, such as a zero-vector, we propose a dynamic baseline [47] that considers the unique characteristics of retinal vasculature, generating more fine-grained explanations. In contrast to natural images, the retinal vasculature adheres to a fixed structure that can be represented in the explanation process. Previous studies indicate variations in capillary density with increasing distance from the FAZ and across different retinal sectors [48]. This implies that distinct characteristics should be considered normal for intercapillary areas and vessels in different areas of the retinal vasculature. Therefore, we select the k -nearest same-type neighbor nodes from the training set and use their feature-wise mean as the dynamic baseline vector x_v^{bl} for each node in a graph. Formally, the baseline vector x_v^{bl} for a node v is defined as

$$x_v^{bl} = \text{avg}(\{x_u \mid u \in \mathcal{N}_l(v)\}). \quad (5)$$

Here $\mathcal{N}_k(v)$ is the k neighborhood of the node v . We define the k neighborhood as the k nodes of *the same type* from the training set with the closest spatial correspondence to node v and x_u is the feature vector of v_u after Z-score normalization. Using the k -nearest-neighbors for creating the baseline vector accommodates local variations at various distances from the fovea. We employ search trees to efficiently identify relevant neighbors in the

training data.

3.3.2. Localization Method

For clinical utility, it is critical that graph nodes that have been identified as important (e.g., individual vessel segments) can be visualized in the corresponding OCTA image. These visualizations can be used to verify whether the extracted retinal characteristics align with the underlying image or if they arise from representation errors, such as image artifacts or segmentation errors. We store the corresponding segmentation map for each node in our graph representation to achieve such a localization.

3.3.3. Explanation Generation

To generate our explanations, we first identify critical nodes using our attribution method by summing over the integrated gradients for the feature vector. The identified critical nodes are then spatially highlighted using the described localization method. Lastly, we identify the decisive characteristics of each critical node using the feature-wise integrated gradients. Examples of the generated spatial and feature-wise explanations are described in Section 4 and visualized in Figure 8.

3.4. Datasets

3.4.1. Proprietary Clinical Dataset

Our OCTA dataset contains 1268 OCTA images of the DVC. For some patients, images of both the right and left eyes are contained in the dataset. Beyond that, no patients are included more than once. DR grades are assigned on a patient level with the stages of *healthy* (847 samples), diabetes mellitus (*DM*) without DR (133 samples), early non-proliferative DR (*early NPDR*, 134 samples), *late NPDR* (62 samples), and *PDR* (92 samples). The disease grades were assigned according to the International Clinical Disease Severity Scale [48], relying on color fundus photography. The OCTA images are 3 mm × 3 mm, with a resolution of 304×304 pixels.

We perform a stratified data split into six parts for our experiments. As sometimes both eyes of a single patient are imaged, we strictly keep both samples in the same split to avoid information leakage. One of the splits is kept as a test set, while the other five splits are used for cross-validation. In each split, *healthy* and *DM* are pooled into a single *healthy* class, and *early NPDR* and *late NPDR* are pooled into a single *NPDR* class. As is typical in a real-world setting, our datasets are imbalanced towards *healthy*

subjects. For these reasons, we evaluate and select our models based on balanced agreement.

3.4.2. Public Dataset

We use the OCTA-500 [49] dataset as an external validation dataset for our method. For that purpose, we use the 200 3 mm \times 3 mm images with a resolution of 304 \times 304 pixels and remove samples with labels other than *DR* or *healthy*. Labels in the OCTA-500 dataset are assigned based on medical patient records. This results in a total of 189 images, of which we use the ILM-OPL projection maps. Notably, these projections contain SVC and DVC vessels, resulting in a slight domain shift compared to our proprietary dataset. Of the 189 images, 160 are healthy samples, and 29 are in the DR class. We apply each algorithmic class’s best-performing checkpoints to classify the OCTA-500 samples. Predictions of *NPDR* and *PDR* are pooled into a single DR class for comparison with the ground truth labels.

3.5. Baseline Methods

We compare our approach to the most prominent and well-performing approaches for DR staging in the literature. These methods include ML using pre-established biomarkers and DL approaches such as CNNs directly operating on the information-rich raw OCTA images. Furthermore, we compare our method to an ophthalmology foundation model that has not previously been employed for this task on OCTA images. Finally, we establish traditional ML methods on graphs that employ global feature aggregation followed by classic ML classifiers without using graph convolutions.

3.5.1. Manual Biomarker Extraction

We extract traditional biomarkers from the image segmentations. We use RF and SVM as classifiers for the DR stage prediction due to their excellent performance in a wide range of applications for tabular data. Specifically, we extract the following biomarkers and use them as classification features:

1. FAZ biomarkers: area, maximal diameter, mean diameter, acircularity index, STD4, and NR300. The reader is referred to [50] for detailed descriptions of the last three biomarkers.
2. Vessel and intercapillary area biomarkers: vessel density, vessel perimeter, and fractal dimension as a vessel complexity measure.

3.5.2. Vision Models

We compare to well-established CNN architectures previously used for the task at hand [51]. We implemented EfficientNet [19], ResNet [17], and VGG [18] models in combination with an optimized data augmentation pipeline. We use all models with weights pre-trained on ImageNet. Beyond these networks, we use the more recent ConvNeXt [52], Efficient Net V2 [53], and SwinTransfomer [54] architectures. We use cross-entropy loss for CNNs and all other neural network architectures.

3.5.3. RETFound Foundational Model

The RETFound model [20] is built on a vision transformer architecture. To initialize this complex architecture’s weights, the model is pre-trained in a self-supervised fashion on more than 900,000 color fundus photography images before being fine-tuned on our training set. We decided to use the color fundus pre-trained model instead of the OCT fine-tuned models due to better performance. This is likely caused by the larger domain shift from en-face OCTA to OCT than to color fundus photography.

3.5.4. Traditional ML on Node Embeddings

Traditional ML on graphs methods are applied to assess the feature quality of node embeddings in our heterogeneous graph. Global aggregation generates a single feature vector for vessel and intercapillary area nodes and the FAZ node. These aggregates are then concatenated and used as input for ML classifiers, with RF and SVM chosen for their effectiveness.

3.6. Metrics

We report *ROC-AUC* for *no DR*, *NPDR*, and *PDR* class staging and for the binary *DR vs no DR* classification. The *class balanced agreement* metric indicates how often the clinical fundus labeling and the OCTA-based stage prediction match. *F1* scores are used to indicate the class-specific agreement rates. Perfect agreement rates for clinical fundus labels and 3mm x 3mm microvascular information are neither expected nor desired. This would disregard the additional microvascular information from OCTA imaging, see 5 and section 4.5.

Table 2: Agreement scores for the staging task into fundus labels *healthy*, *NPDR* and *PDR*. The data representation describes the information used as input to the subsequent classifier. Results are obtained on a test set that was separated before cross-validation. Standard deviations are calculated based on the results from the 5-fold cross-validation. We report p-values for paired t-tests with the heterogeneous graph model in parentheses after the standard deviations.

Architecture	Data Representation	Model	ROC AUC	Balanced Agreement	F1 Healthy	F1 NPDR	F1 PDR	DR vs no DR ROC AUC
Trad. ML	Tabular Biomarkers	RF	0.796 ±0.014(.02)	0.639 ±0.018(.01)	0.843 ±0.017(.09)	0.421 ±0.019(.47)	0.490 ±0.035(.05)	0.862 ±0.007(.14)
		SVM	0.776 ±0.012(.03)	0.615 ±0.024(.01)	0.831 ±0.028(.07)	0.395 ±0.062(.33)	0.440 ±0.085(.04)	0.867 ±0.010(.49)
CNN	Image DVC	VGG11	0.822 ±0.008(.35)	0.661 ±0.024(.05)	0.870 ±0.043(.03)	0.443 ±0.127(.35)	0.522 ±0.025(.14)	0.874 ±0.010(.05)
		ResNet18	0.801 ±0.024(.07)	0.633 ±0.034(.04)	0.861 ±0.012(.01)	0.414 ±0.067(.44)	0.466 ±0.048(.06)	0.872 ±0.009(.13)
		Eff. Net B0	0.818 ±0.021(.30)	0.652 ±0.034(.10)	0.873 ±0.034(.01)	0.370 ±0.055(.17)	0.514 ±0.038(.17)	0.875 ±0.014(.12)
		ResNet50	0.788 ±0.018(.02)	0.587 ±0.025(.01)	0.894 ±0.016(.01)	0.288 ±0.066(.03)	0.425 ±0.018(.02)	0.866 ±0.014(.43)
		Eff. Net V2 s	0.807 ±0.031(.05)	0.663 ±0.040(.01)	0.888 ±0.020(.01)	0.433 ±0.081(.35)	0.549 ±0.066(.18)	0.853 ±0.031(.20)
		ConvNeXt s	0.822 ±0.018(.37)	0.654 ±0.026(.05)	0.898 ±0.020(.01)	0.376 ±0.073(.22)	0.503 ±0.046(.10)	0.876 ±0.014(.11)
	Image SVC	ConvNeXt s	0.804 ±0.019(.12)	0.623 ±0.032(.01)	0.893 ±0.015(.01)	0.405 ±0.067(.38)	0.494 ±0.043(.04)	0.881 ±0.016(.06)
	Seg. DVC	ConvNeXt s	0.813 ±0.015(.22)	0.652 ±0.026(.04)	0.877 ±0.021(.01)	0.400 ±0.071(.34)	0.554 ±0.061(.42)	0.862 ±0.015(.25)
	Transformer	Image	RETFound ±0.008(.31)	0.638 ±0.021(.01)	0.836 ±0.032(.16)	0.362 ±0.078(.13)	0.532 ±0.021(.14)	0.871 ±0.007(.13)
		SwinTrans.	0.781 ±0.042(.06)	0.556 ±0.125(.04)	0.887 ±0.017(.01)	0.312 ±0.204(.15)	0.418 ±0.238(.15)	0.846 ±0.041(.17)
Trad. ML	Node Embeddings	RF	0.828 ±0.010(.49)	0.658 ±0.007(.04)	0.834 ±0.006(.11)	0.362 ±0.031(.08)	0.560 ±0.020(.43)	0.870 ±0.007(.19)
		SVM	0.776 ±0.012(.03)	0.615 ±0.024(.01)	0.831 ±0.028(.07)	0.395 ±0.062(.33)	0.440 ±0.085(.04)	0.867 ±0.010(.49)
Heterogeneous Graph Learning	Graph	Ours	0.829 ±0.037	0.696 ±0.034	0.819 ±0.021	0.419 ±0.057	0.568 ±0.090	0.867 ±0.003

4. DR Staging Experiments

4.1. Agreement Rates of Machine Learning OCTA Grading Approaches

Our biology-informed heterogeneous graph representation achieves comparable ROC AUC scores of 0.829, matching the best CNN (0.822) and transformer models (0.819). Staging purely based on established biomarkers reaches notably lower agreement with the CFP-based labels. We attribute the lower agreement to the lack of biomarkers that fully encode pathological information on intraretinal microvascular abnormalities and microaneurysms. In contrast, CNNs and our heterogeneous graph representation plateau at agreement rates where the DR stage is determined by microvascular information in OCTA images that diverges from clinical evaluation through CFP (see Figure 5).

Table 3: Classification performance for the binary classification into *healthy* versus DR. The results are obtained on the external OCTA-500 without further fine-tuning the models previously trained on the other reported dataset. The checkpoint from the 5-fold cross-validation on the proprietary dataset with the highest balanced agreement is used for evaluation on the OCTA-500 dataset.

Architecture	Data Rep.	Model	Bal. Agr.	F1 Heal.	F1 DR	AUC ROC	AUC PRC
Trad. ML	Tabular Biom.	RF	0.821	0.963	0.760	0.960	0.872
		SVM	0.806	0.947	0.691	0.876	0.773
CNN	Image	VGG11	0.773	0.958	0.696	0.942	0.873
		ResNet18	0.586	0.930	0.294	0.920	0.785
		Eff. Net B0	0.707	0.950	0.585	0.862	0.778
Transformer	Image	RETFound	0.746	0.915	0.558	0.777	0.628
Trad. ML	Node Embed.	RF	0.839	0.967	0.785	0.916	0.857
		SVM	0.500	0.000	0.266	0.289	0.111
Heterogeneous Graph Learning	Graph	Ours	0.893	0.978	0.868	0.952	0.909

4.2. Sensitivity analysis on OCTA image variations and segmentation maps

A comparison of using the SVC instead of the DVC using the same CNN architecture shows similar staging performance for using either the DVC or the SVC layer. Moreover, we experimented with directly using segmentation maps as input to the CNN classifier. Interestingly, this results in comparable performance to raw images and opens an interesting avenue for enhancing explainability in classification with CNN models.

4.3. Generalization to public OCTA-500 dataset

We use the checkpoints with the highest class-balanced agreement rates from the 5-fold cross-validation on the proprietary dataset for evaluation on the OCTA-500 dataset. Our proposed graph learning method yields the highest agreement with the medical record labels in this 0-shot evaluation on the OCTA-500 dataset (see Table 3). This highlights the robustness of our approach to minor domain changes induced by different hardware (OCTA scanners) and preprocessing algorithms (e.g., layer segmentation and intensity clipping). The performance between the CNN models and the RET-Found model differs strongly, probably due to differences in the high-level concepts used by the vision models. Due to their lack of interpretability, the underlying mechanisms that cause the model to fail cannot be identified. The simple random forest models perform excellently in this generalization

task. VGG11 and ResNet18 exhibit high AUC ROC values compared to their relatively low balanced agreement. This indicates that while these models are successful in differentiating the disease level, the classification threshold does not generalize to the new dataset.

Table 4: Comparison for using vessel graph, intercapillary area graph, and heterogeneous graph

Data Representation	Model	ROC AUC	Bal. Agr.	F1 Healthy	F1 NPD _R	F1 PDR	DR vs no DR ROC AUC
Vessel Graph	GNN	0.828 ±0.005	0.642 ±0.025	0.812 ±0.037	0.372 ±0.060	0.516 ±0.048	0.876 ±0.010
Intercapillary Area Graph	GNN	0.815 ±0.018	0.627 ±0.043	0.836 ±0.047	0.336 ±0.178	0.498 ±0.068	0.881 ±0.012
Heterogeneous Graph	GNN	0.829 ±0.037	0.696 ±0.034	0.819 ±0.021	0.419 ±0.057	0.568 ±0.090	0.867 ±0.003

4.4. Comparison to Homogeneous Graph Representations

We experimented with a simplified setting of the individual homogeneous graph representations and included the results below in Table 4. The intercapillary region graph does not achieve comparable agreement rates measured by ROC AUC (0.815), compared to both vessel (0.828) and heterogeneous graphs (0.829). We attribute this to the lack of information about intraretinal microvascular abnormalities and microaneurysms. The performance of the vessel graph is comparable to the performance of the heterogeneous graph. In fact, the vessel graph can indirectly encode the crucial pathological non-perfusion information through a reduction in total vessel area. However, only the heterogeneous graph allows for a direct attribution to the non-perfusion regions and therefore the absence of capillaries.

4.5. Expert reading of OCTA predictions that disagree with clinical fundus stage labels

DR stage labels in the proprietary dataset were assigned according to the International Clinical Disease Severity Scale [55] based on the Early Treatment Diabetic Retinopathy Study (ETDRS), which relies on color fundus photography. This feature-based grading approach does not necessarily align with the microvasculature changes visible in OCTA images [56]. Pathological microvascular alterations can occur without microaneurysms observable on fundus photography, a phenomenon we encountered frequently in our dataset.

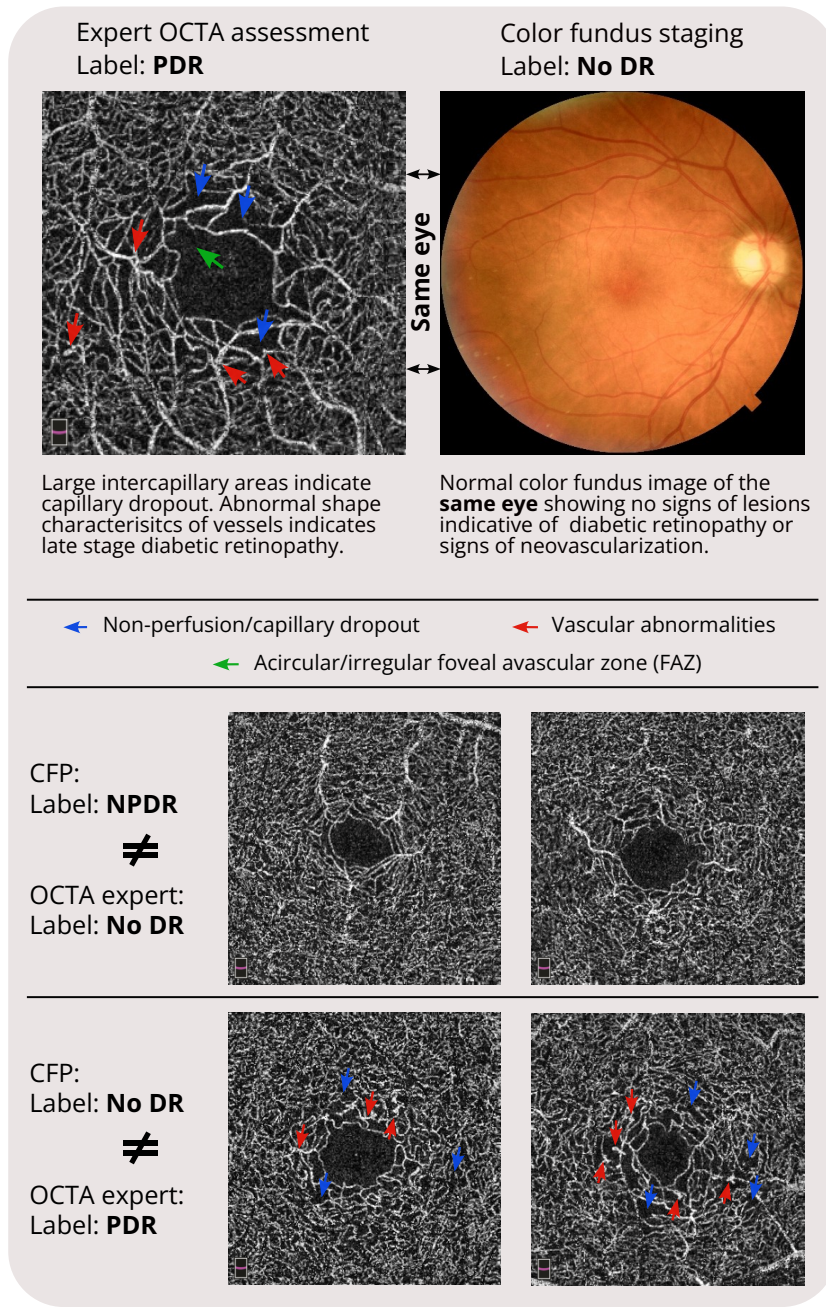


Figure 5: Overview of cases where the microvascular changes assessed using en face OCTA images do not align with the disease progression information obtained from color fundus photography (CFP). (top row) Comparison of an en face OCTA image with the matching CFP image (middle and bottom row). Further cases of OCTA images where the OCTA-based expert assessment does not align with CFP grading.

To investigate these staging discrepancies, we performed staging experiments with a senior ophthalmologist with over ten years of OCTA and DR experience. Nine cases were preselected where OCTA model predictions plausibly disagreed with fundus labels (see Section 5). Expert review confirmed the disagreement in eight of these cases. We report cases where expert ophthalmologists assess OCTA images as NPDR or even PDR stage, while no retinopathy is detected in the corresponding fundus images (see Figure 5 first and last row). Conversely, sometimes no microvascular abnormalities are visible in the spatially limited 3 mm x 3 mm OCTA image, while the color fundus examination indicates the DR (see Figure 5 middle row).

In clinical practice, such modality discordance between fundus and OCTA labels is particularly relevant, as clinicians must reconcile information from both imaging techniques to formulate unified staging and treatment decisions.

5. Interpretability Analysis and Explainability of Staging

5.1. Feature Relation to Microvascular Pathologies

Our feature embeddings for intercapillary areas, vessel segments, and the FAZ are directly linked to pathological changes of the microvasculature. Figure 6 illustrates the relationship between specific features and the progression of DR. The increase in tortuosity of vessels is defined as a microvascular abnormality; we observe a clear increase in the 90% quantile tortuosity of vessel segments (Figure 6 top left). Capillary degeneration results in less branching and therefore larger vessel segments; moreover, microaneurysms and neovascularizations often appear as large segmented vessel segments. An increased 90% quantile for vessel segment volume clearly reflects these pathological changes (Figure 6 top center). Microvascular abnormalities and microaneurysms are characterized by irregular shapes. We observe that the 90% quantile of the radius variability of isolated vessel segments is increased for the NPDR and PDR stage (Figure 6 top right). Capillary loss is best reflected in the characteristics of intercapillary areas. We see a clear increase in the median area of intercapillary areas (Figure 6 middle left), and even more drastically for the 90% quantile (Figure 6 middle center). This capillary loss is also reflected in other characteristics, such as the increased median major axis length of intercapillary areas (Figure 6 middle right). Changes to the FAZ characteristics, due to the loss of integrity of parafoveal vessels, are a known indicator for the progression of DR. We see this effect most pronounced in the decreased solidity (defined as the ratio of the area of a region

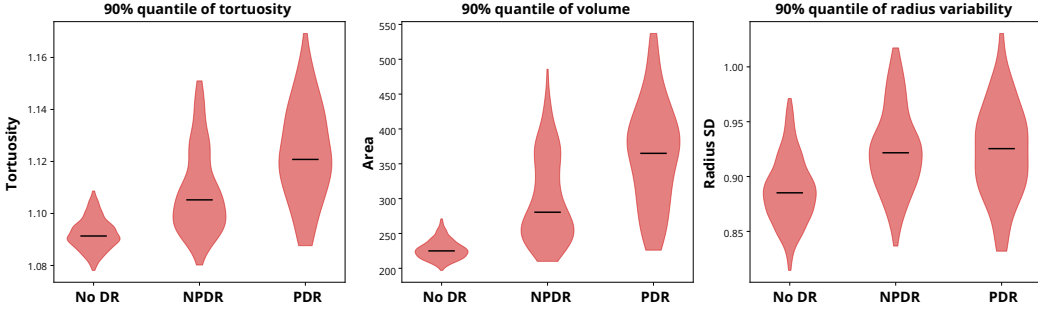
to the area of its convex hull) (Figure 6 bottom left). Changes, although less pronounced, are also visible in the area and the length of the minor axis of the FAZ (Figure 6 bottom center and right).

5.2. Examples for spatial explanations

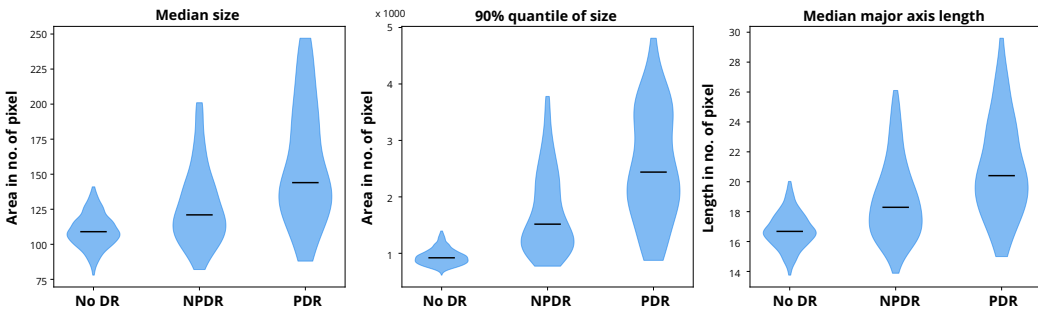
To illustrate that (1) our method links pathological microvascular changes to the stage prediction task, and (2) our method allows traceable prediction results, we show explanations for predicted DR stages. Our method allows the spatially exact identification of the most important vessel segments and intercapillary areas for the DR stage prediction task. Figure 7 shows two examples where the most important vessel segments and intercapillary areas are highlighted for two patients suffering from DR. The precise spatial attribution is in stark contrast to common CNN explanations, which often provide broad and scattered explanations that do not allow for a precise attribution to abnormal vessels, areas of capillary dropout, or microaneurysms, guiding the prediction. We adopt explainability approaches previously employed by Ryu et al. [11] and Heisler et al. [10] and use grad-CAM to create model explanations. The grad-CAM explanations are focused on the center of the FAZ, which is unrelated to DR disease progression. Similarly, a majority of the area highlighted by integrated gradients, combined with the vision models, highlights areas within the FAZ. For the subject in 7 a) where the model prediction on OCTA deviates from the clinical fundus grading, both vision explanations do not provide an interpretable explanation for the prediction of the further progressed DR stage. In contrast, our methods clearly highlight vessel segments that resemble abnormal structures that guide the model to predict late-stage DR, deviating from the fundus-based diagnosis.

Beyond the spatial explanations, our method enables us to attribute the elevated importance of specific nodes to high-level concepts, such as vessel tortuosity or intercapillary area size, that are directly linked to disease progression. We display three different examples: Figure 8 a) shows an example where the clinical label is no DR while the OCTA-based prediction as well as the OCTA expert label indicate PDR, Figure 8 b) displays an image that was classified as PDR with clinical label PDR, and Figure 8 c) displays an image that was classified as NPDR with clinical label NPDR. We indicate the most important characteristics and their deviation from the norm for exemplary nodes. Additionally, we provide full interactive explanations in our code repository, which allows us to see the influence of intercapillary areas, the FAZ, vessel segments, and their characteristics on the predicted DR

Vessel Characteristics



Intercapillary Area Characteristics



FAZ Characteristics

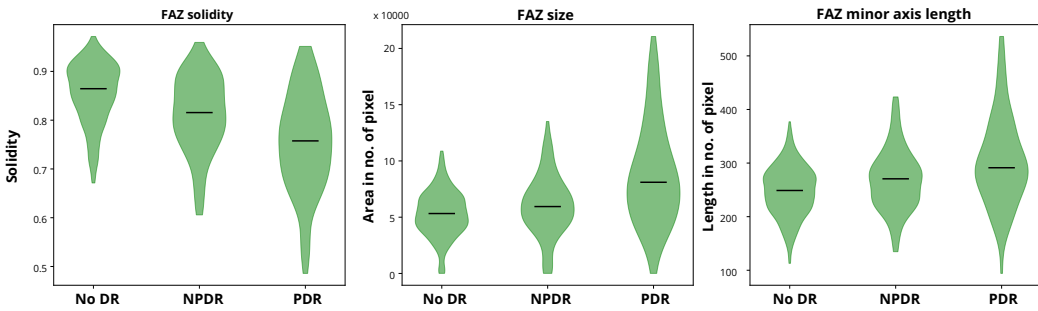


Figure 6: Analysis of specific features that are encoded in our heterogeneous graph representation for vessel segments (top row), intercapillary areas (middle row), and the FAZ (bottom row). Violin plots are stratified by clinical DR grade. The violin plots show the distribution of a specific characteristic (e.g., median intercapillary area size) across all OCTA scans of the specified disease stage.

stage.

Example a) in Figure 8 shows the OCTA image of a subject with no DR following standard fundus examination. The OCTA image was graded with the PDR stage by an expert ophthalmologist. Our model aligns with the OCTA expert analysis, highlighting the intercapillary areas around the FAZ

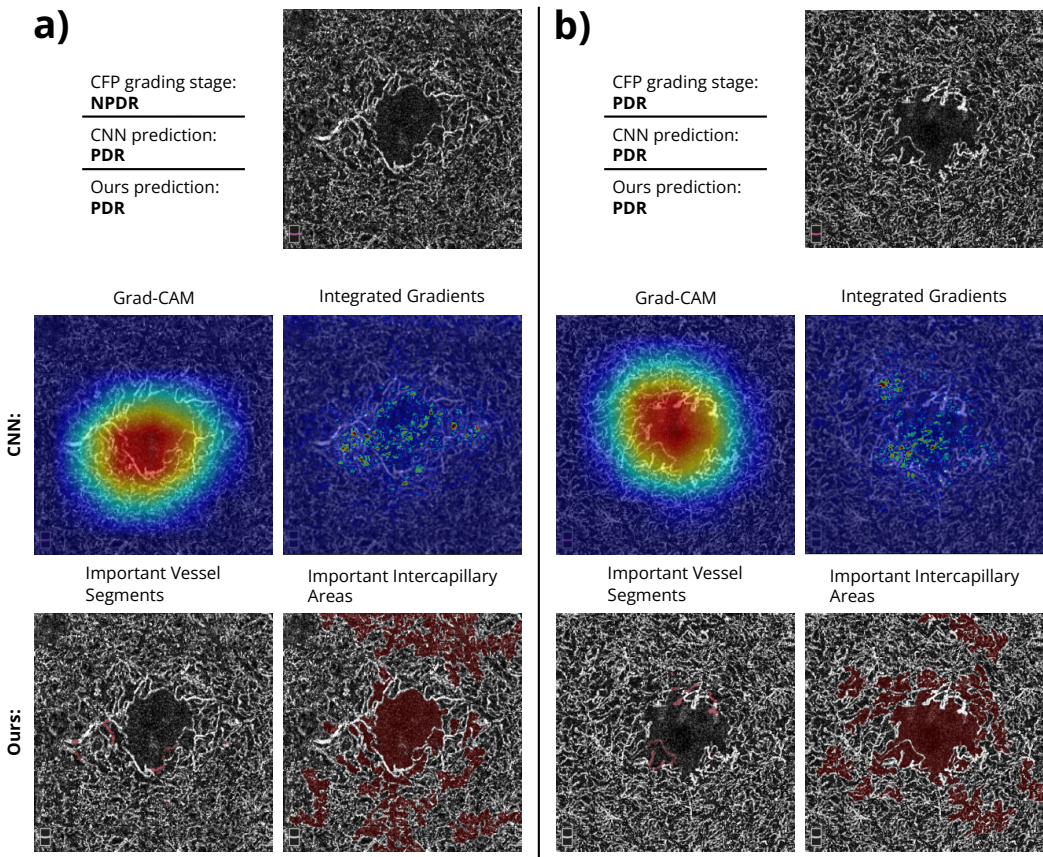


Figure 7: Comparison of different explainability tools for the DR staging task on OCTA images. GradCAM and integrated gradients are state-of-the-art approaches that previous works have applied to DR staging. Sample a) describes a sample with clinical diagnosis *NPDR* that the CNN and graph classification model both classify as *PDR*. Sample b) describes a sample with clinical diagnosis *PDR* that the CNN and graph classification model both also identify as *PDR*. Compared to traditional spatial explanations for vision models, our framework (bottom row) enables the precise localization of critical vessel segments with shape and intensity that indicate intraretinal microvascular abnormalities and perfused microaneurysms. Intercapillary areas indicate image areas where our model sees reduced capillary density.

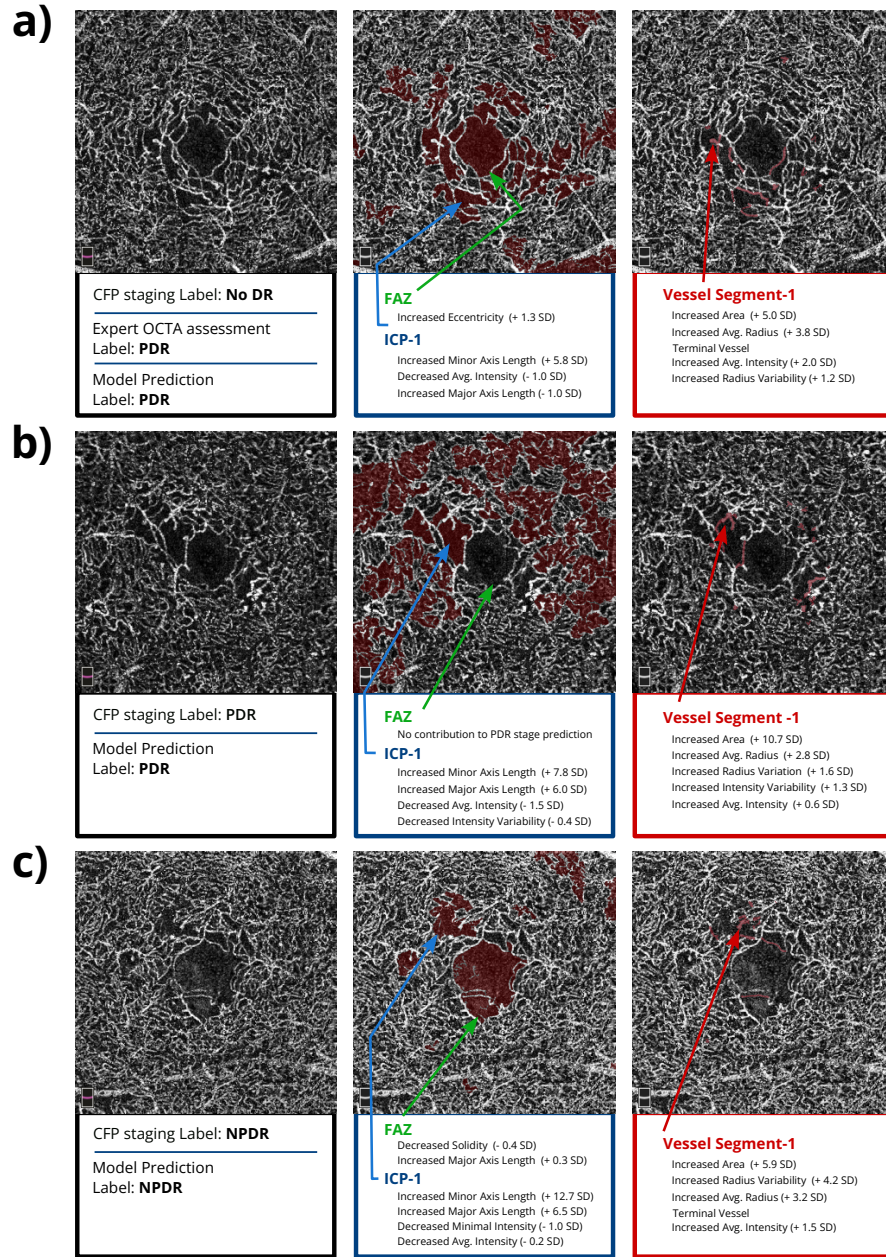


Figure 8: Explanations for model predictions and explanations of our framework with predicted stages agreeing to color fundus staging (b, c)), and an example with diverging prediction (a)). Red overlay indicates contribution of intercapillary areas, FAZ (center column), or vessel segments (right column) to the predicted stage. Boxes below the images indicate which features are most important to the prediction, and how they diverge from the norm.

as highly important, due to their increased size (e.g., minor axis length and major axis length) and their low average image intensity. The eccentricity of the FAZ also contributed to the stage prediction. Moreover, specific vessel segments contribute to the PDR diagnosis, such as the bright intensity terminal vessel emphasized by the red arrow. In the prediction, the size (area and average radius), shape abnormality (increased radius variability), hyperintensity, and the terminal position are the most important characteristics.

Example b) in Figure 8 shows an example where the clinical stage is PDR, aligning with the severity of the microvascular changes in the OCTA image. While the FAZ does not indicate the PDR stage, the large size and low intensity in the capillary areas are indicative of the PDR stage. Moreover, the model identifies multiple abnormally shaped vessels, such as the vessel segment indicated by the red arrow, which exhibits increased size (area + radius), atypical shape characteristics (increased radius variability), and unusually high variation of intensity within the segment.

Finally, example c) in Figure 8 shows the OCTA image of a subject with clinical label NPDR and model prediction NPDR. The decreased solidity of the FAZ and the slightly increased (+0.3 SD) major axis length contribute to the NPDR prediction. Moreover, some intercapillary areas contribute to the DR prediction through increased size and decreased intensity. The vessel segment indicated by the red arrow, which shows strong similarities to a microaneurysm, strongly contributes to the NPDR diagnosis through size (area and radius), shape (radius variability), hyperintensity, and terminal position.

Notably, the baselines, as depicted in Figure 7, are limited to spatial explanations. In contrast to our framework, they do not offer feature-wise attributions towards interpretable concepts (see Figure 8). Therefore, our comparison is limited to these spatial explanations.

5.3. Comparison to Other Graph-Based Explanations

Random forest and support vector machine classifiers on aggregated node embeddings come with the disadvantage of losing spatial information for explainability. The aggregation of node information followed by an ensemble of decision trees in random forests does not allow spatial hinting towards critical regions.

Homogeneous graph representations do not allow for a direct attribution towards clinically well-studied microvascular changes. Using vessel graphs alone does not allow direct attribution to regions of ischemia and capillary

dropout, which are hallmarks of DR. Using intercapillary areas alone does not allow attribution to intraretinal microvascular abnormalities, which are the second pillar for the analysis of DR in OCTA images. Only the combination of both representations provides the capability to attribute the classification directly to the microvascular changes that comprise dropout, abnormalities, and new-growth of vessels.

6. Discussion

In this work, we propose an interpretable method for DR staging support using OCTA images. We establish a specialized heterogeneous graph representation that models the particularities of the retinal vasculature. Building on this novel data representation, we develop an efficient GNN model that solves DR staging as a graph classification task. Finally, we introduce an interpretability tool providing fine-grained explanations for our predictions using spatial explanations that highlight critical structures and attribute their importance to specific characteristics.

Our staging approach provides a notable step towards interpretable disease staging of OCTA images, which is crucial for adapting discriminative models in clinical practice. While our method improves existing explainability frameworks, we have not created a perfectly interpretable classification pipeline. Our improvements concern perspective and mathematical interpretability. Perspective interpretability is improved by the fine-grained spatial explanations that allow us to precisely visualize important vessels and intercapillary areas, which has been impossible for CNNs and vision transformers. Moreover, our attributions consist of human-interpretable concepts that are commonly associated with disease progression. By introducing a data representation based on the retinal vasculature, we restrict our model to these anatomical constraints in decision-making. We improve mathematical interpretability by limiting learnable parameters and network layers [57]. Nevertheless, our model consists of multiple layers with activations and numerous features, which allows for non-trivial feature interaction. Therefore, the study of feature interaction, which has been previously done for MLPs [58], is a necessary future work.

Although our approach avoids using the largely uninterpretable CNN and transformer models for the classification stage, it still relies on these architectures to generate high-quality segmentations. Utilizing this class of networks in the data representation stage provides some advantages compared to the

usage at a later stage. The first advantage is the enhanced interpretability of the algorithmic outcomes using the abstracted representation. The second advantage is that the vision models can be trained on existing large-scale synthetic datasets [15] compared to the disease classification task, where high-quality data is still limited. A limitation persists in the susceptibility of the graph representation to segmentation errors. However, we argue that single-stage CNN or vision transformer models would implicitly create internal representations similar to a segmentation and, therefore, may be similarly affected. Moreover, segmentation errors are easier to detect than reasoning about erroneous internal representations in CNNs and vision transformers.

Beyond image classification, we believe that our representation is a foundation for future applications, such as link prediction for correcting erroneous segmentation and node classification of intercapillary areas or vessel segments, e.g., for the identification of microaneurysms, intraretinal microvascular abnormalities, and neovascularization.

Appendix A. Acknowledgements

Appendix A.1. Funding

This research did not receive any specific grant from funding agencies in the public, commercial, or not-for-profit sectors.

Appendix A.2. Generative AI

We used large language models at the sentence level to improve formulations and correct spelling and grammar.

References

- [1] Z. L. Teo, Y.-C. Tham, M. Yu, M. L. Chee, T. H. Rim, N. Cheung, M. M. Bikbov, Y. X. Wang, Y. Tang, Y. Lu, et al., Global prevalence of diabetic retinopathy and projection of burden through 2045: systematic review and meta-analysis, *Ophthalmology* 128 (11) (2021) 1580–1591.
- [2] Z. Sun, F. Tang, R. Wong, J. Lok, S. K. Szeto, J. C. Chan, C. K. Chan, C. C. Tham, D. S. Ng, C. Y. Cheung, OCT angiography metrics predict progression of diabetic retinopathy and development of diabetic macular edema: a prospective study, *Ophthalmology* 126 (12) (2019) 1675–1684.

- [3] D. Le, T. Son, X. Yao, Machine learning in optical coherence tomography angiography, *Experimental Biology and Medicine* 246 (20) (2021) 2170–2183.
- [4] A. E. Fayed, M. J. Menten, L. Kreitner, J. C. Paetzold, D. Rueckert, S. M. Bassily, R. R. Fikry, A. M. Hagag, S. Sivaprasad, Retinal vasculature of different diameters and plexuses exhibit distinct vulnerability in varying severity of diabetic retinopathy, *Eye* (2024) 1–8.
- [5] J. Moore, S. Bagley, G. Ireland, D. McLeod, M. Boulton, Three dimensional analysis of microaneurysms in the human diabetic retina, *The Journal of Anatomy* 194 (1) (1999) 89–100.
- [6] S. Stolte, R. Fang, A survey on medical image analysis in diabetic retinopathy, *Medical image analysis* 64 (2020) 101742.
- [7] M. Alam, D. Le, J. I. Lim, R. V. Chan, X. Yao, Supervised machine learning based multi-task artificial intelligence classification of retinopathies, *Journal of clinical medicine* 8 (6) (2019) 872.
- [8] H. S. Sandhu, M. Elmogy, A. T. Sharafeldeen, M. Elsharkawy, N. El-Adawy, A. Eltanboly, A. Shalaby, R. Keynton, A. El-Baz, Automated diagnosis of diabetic retinopathy using clinical biomarkers, optical coherence tomography, and optical coherence tomography angiography, *American journal of ophthalmology* 216 (2020) 201–206.
- [9] M. Alam, Y. Zhang, J. I. Lim, R. V. Chan, M. Yang, X. Yao, Quantitative optical coherence tomography angiography features for objective classification and staging of diabetic retinopathy, *Retina* 40 (2) (2020) 322–332.
- [10] M. Heisler, S. Karst, J. Lo, Z. Mammo, T. Yu, S. Warner, D. Maberley, et al., Ensemble deep learning for diabetic retinopathy detection using optical coherence tomography angiography, *Translational Vision Science & Technology* 9 (2) (2020) 20–20.
- [11] G. Ryu, K. Lee, D. Park, S. H. Park, M. Sagong, A deep learning model for identifying diabetic retinopathy using optical coherence tomography angiography, *Scientific reports* 11 (1) (2021) 23024.

- [12] P. Zang, T. T. Hormel, X. Wang, K. Tsuboi, D. Huang, T. S. Hwang, Y. Jia, A diabetic retinopathy classification framework based on deep-learning analysis of OCT angiography, *Translational vision science & technology* 11 (7) (2022) 10–10.
- [13] B. Zhou, A. Khosla, A. Lapedriza, A. Oliva, A. Torralba, Learning deep features for discriminative localization, in: *CVPR*, 2016, pp. 2921–2929.
- [14] R. R. Selvaraju, M. Cogswell, A. Das, R. Vedantam, D. Parikh, D. Batra, Grad-cam: Visual explanations from deep networks via gradient-based localization, in: *ICCV*, 2017, pp. 618–626.
- [15] L. Kreitner, J. C. Paetzold, N. Rauch, C. Chen, A. M. Hagag, A. E. Fayed, S. Sivaprasad, S. Rausch, J. Weichsel, B. H. Menze, et al., Detailed retinal vessel segmentation without human annotations using simulated optical coherence tomography angiographs, *arXiv preprint arXiv:2306.10941* (2023).
- [16] D. Y. Kim, J. Fingler, J. S. Werner, D. M. Schwartz, S. E. Fraser, R. J. Zawadzki, In vivo volumetric imaging of human retinal circulation with phase-variance optical coherence tomography, *Biomedical optics express* 2 (6) (2011) 1504–1513.
- [17] S. Xie, R. Girshick, P. Dollár, Z. Tu, K. He, Aggregated residual transformations for deep neural networks, in: *CVPR*, 2017, pp. 1492–1500.
- [18] K. Simonyan, A. Zisserman, Very deep convolutional networks for large-scale image recognition, *arXiv preprint arXiv:1409.1556* (2014).
- [19] M. Tan, Q. Le, Efficientnet: Rethinking model scaling for convolutional neural networks, in: *ICML*, PMLR, 2019, pp. 6105–6114.
- [20] Y. Zhou, M. A. Chia, S. K. Wagner, M. S. Ayhan, D. J. Williamson, R. R. Struyven, T. Liu, M. Xu, M. G. Lozano, P. Woodward-Court, et al., A foundation model for generalizable disease detection from retinal images, *Nature* (2023) 1–8.
- [21] P. Velickovic, G. Cucurull, A. Casanova, A. Romero, P. Lio, Y. Bengio, et al., Graph attention networks, *stat 1050* (20) (2017) 10–48550.

- [22] T. N. Kipf, M. Welling, Semi-supervised classification with graph convolutional networks, arXiv preprint arXiv:1609.02907 (2016).
- [23] W. Hamilton, Z. Ying, J. Leskovec, Inductive representation learning on large graphs, *Advances in neural information processing systems* 30 (2017).
- [24] J. Zhou, G. Cui, S. Hu, Z. Zhang, C. Yang, Z. Liu, L. Wang, C. Li, M. Sun, Graph neural networks: A review of methods and applications, *AI open* 1 (2020) 57–81.
- [25] H. Zhang, R. Song, L. Wang, L. Zhang, D. Wang, C. Wang, W. Zhang, Classification of brain disorders in rs-fmri via local-to-global graph neural networks, *IEEE transactions on medical imaging* 42 (2) (2022) 444–455.
- [26] C. Prabhakar, H. B. Li, J. C. Paetzold, T. Loehr, C. Niu, M. Mühlau, D. Rueckert, B. Wiestler, B. Menze, Self-pruning graph neural network for predicting inflammatory disease activity in multiple sclerosis from brain mr images, in: *MICCAI*, Springer, 2023, pp. 226–236.
- [27] J. C. Paetzold, J. McGinnis, S. Shit, I. Ezhov, P. Büschl, C. Prabhakar, A. Sekuboyina, M. Todorov, G. Kaassis, A. Ertürk, et al., Whole brain vessel graphs: A dataset and benchmark for graph learning and neuroscience, in: *NeurIPS*, 2021.
- [28] H. Wang, G. Huang, Z. Zhao, et al., CCF-GNN: A unified model aggregating appearance, microenvironment, and topology for pathology image classification, *IEEE Transactions on Medical Imaging* (2023).
- [29] P. E. Pope, S. Kolouri, M. Rostami, C. E. Martin, H. Hoffmann, Explainability methods for graph convolutional neural networks, in: *CVPR*, 2019, pp. 10772–10781.
- [30] Z. Ying, D. Bourgeois, J. You, M. Zitnik, J. Leskovec, Gnnexplainer: Generating explanations for graph neural networks, *NeurIPS* 32 (2019).
- [31] Q. Huang, M. Yamada, Y. Tian, D. Singh, Y. Chang, Graphlime: Local interpretable model explanations for graph neural networks, *IEEE Transactions on Knowledge and Data Engineering* (2022).

- [32] M. T. Ribeiro, S. Singh, C. Guestrin, " why should i trust you?" explaining the predictions of any classifier, in: SIGKDD, 2016, pp. 1135–1144.
- [33] H. Yuan, H. Yu, S. Gui, S. Ji, Explainability in graph neural networks: A taxonomic survey, *IEEE transactions on pattern analysis and machine intelligence* 45 (5) (2022) 5782–5799.
- [34] C. Agarwal, O. Queen, H. Lakkaraju, M. Zitnik, Evaluating explainability for graph neural networks, *Scientific Data* 10 (1) (2023) 144.
- [35] M. J. Menten, L. Kreitner, J. C. Paetzold, A. M. Hagag, S. M. Bassily, S. Sivaprasad, D. Rueckert, A. E. Fayed, Synthetic data facilitates deep-learning-based segmentation of OCT angiography images without human annotations, *Investigative Ophthalmology & Visual Science* 64 (8) (2023) 5450–5450.
- [36] J. C. Paetzold, L. Lux, L. Kreitner, I. Ezhov, S. Shit, A. J. Lotery, M. J. Menten, D. Rueckert, Geometric deep learning for disease classification in OCTA images, *Investigative Ophthalmology & Visual Science* 64 (8) (2023) 1098–1098.
- [37] M. I. Todorov, J. C. Paetzold, O. Schoppe, G. Tetteh, S. Shit, V. Efremov, K. Todorov-Völgyi, M. Düring, M. Dichgans, M. Piraud, et al., Machine learning analysis of whole mouse brain vasculature, *Nature methods* 17 (4) (2020) 442–449.
- [38] D. Drees, A. Scherzinger, R. Hägerling, F. Kiefer, X. Jiang, Scalable robust graph and feature extraction for arbitrary vessel networks in large volumetric datasets, *BMC bioinformatics* 22 (1) (2021) 1–28.
- [39] J. Meyer-Spradow, T. Ropinski, J. Mensmann, K. Hinrichs, Voreen: A rapid-prototyping environment for ray-casting-based volume visualizations, *IEEE Computer Graphics and Applications* 29 (6) (2009) 6–13.
- [40] J. Schottenhamml, E. M. Moult, S. Ploner, B. Lee, E. A. Novais, E. Cole, S. Dang, C. D. Lu, L. Husvogt, N. K. Waheed, et al., An automatic, intercapillary area based algorithm for quantifying diabetes related capillary dropout using OCT angiography, *Retina* 36 (Suppl 1) (2016) S93.
- [41] N. Terada, T. Murakami, A. Uji, K. Ishihara, Y. Dodo, K. Nishikawa, K. Morino, A. Tsujikawa, The intercapillary space spectrum as a marker

of diabetic retinopathy severity on optical coherence tomography angiography, *Scientific Reports* 12 (1) (2022) 3089.

- [42] Z. Sun, D. Yang, Z. Tang, D. S. Ng, C. Y. Cheung, Optical coherence tomography angiography in diabetic retinopathy: an updated review, *Eye* 35 (1) (2021) 149–161.
- [43] J. Conrath, R. Giorgi, D. Raccah, B. Ridings, Foveal avascular zone in diabetic retinopathy: quantitative vs qualitative assessment, *Eye* 19 (3) (2005) 322–326.
- [44] M. Fey, J. E. Lenssen, Fast graph representation learning with pytorch geometric, *arXiv preprint arXiv:1903.02428* (2019).
- [45] M. Sundararajan, A. Taly, Q. Yan, Axiomatic attribution for deep networks, in: *ICML, PMLR*, 2017, pp. 3319–3328.
- [46] K. McCloskey, A. Taly, F. Monti, M. P. Brenner, L. J. Colwell, Using attribution to decode binding mechanism in neural network models for chemistry, *Proceedings of the National Academy of Sciences* 116 (24) (2019) 11624–11629.
- [47] P. Sturmfels, S. Lundberg, S.-I. Lee, Visualizing the impact of feature attribution baselines, *Distill* 5 (1) (2020) e22.
- [48] C. Lavia, P. Mecê, M. Nassisi, S. Bonnin, J. Marie-Louise, A. Couturier, A. Erginay, R. Tadayoni, A. Gaudric, Retinal capillary plexus pattern and density from fovea to periphery measured in healthy eyes with swept-source optical coherence tomography angiography, *Scientific reports* 10 (1) (2020) 1474.
- [49] M. Li, K. Huang, Q. Xu, J. Yang, Y. Zhang, Z. Ji, K. Xie, S. Yuan, Q. Liu, Q. Chen, OCTA-500: A retinal dataset for optical coherence tomography angiography study, *arXiv e-prints* (2020) arXiv–2012.
- [50] Y. Lu, J. M. Simonett, J. Wang, M. Zhang, T. Hwang, A. M. Hagag, D. Huang, D. Li, Y. Jia, Evaluation of automatically quantified foveal avascular zone metrics for diagnosis of diabetic retinopathy using optical coherence tomography angiography, *Investigative ophthalmology & visual science* 59 (6) (2018) 2212–2221.

- [51] B. Qian, H. Chen, X. Wang, H. Che, G. Kwon, J. Kim, S. Choi, S. Shin, F. Krause, M. Unterdechler, et al., DRAC: Diabetic retinopathy analysis challenge with ultra-wide optical coherence tomography angiography images, arXiv preprint arXiv:2304.02389 (2023).
- [52] Z. Liu, H. Mao, C.-Y. Wu, C. Feichtenhofer, T. Darrell, S. Xie, A convnet for the 2020s, in: Proceedings of the IEEE/CVF conference on computer vision and pattern recognition, 2022, pp. 11976–11986.
- [53] M. Tan, Q. Le, Efficientnetv2: Smaller models and faster training, in: International conference on machine learning, PMLR, 2021, pp. 10096–10106.
- [54] Z. Liu, Y. Lin, Y. Cao, H. Hu, Y. Wei, Z. Zhang, S. Lin, B. Guo, Swin transformer: Hierarchical vision transformer using shifted windows, in: Proceedings of the IEEE/CVF international conference on computer vision, 2021, pp. 10012–10022.
- [55] C. P. Wilkinson, F. L. Ferris III, R. E. Klein, P. P. Lee, C. D. Agardh, M. Davis, D. Dills, A. Kampik, R. Pararajasegaram, J. T. Verdaguer, et al., Proposed international clinical diabetic retinopathy and diabetic macular edema disease severity scales, *Ophthalmology* 110 (9) (2003) 1677–1682.
- [56] I. A. Thompson, A. K. Durrani, S. Patel, Optical coherence tomography angiography characteristics in diabetic patients without clinical diabetic retinopathy, *Eye* 33 (4) (2019) 648–652.
- [57] P. Barceló, M. Monet, J. Pérez, B. Subercaseaux, Model interpretability through the lens of computational complexity, *NeurIPS* 33 (2020) 15487–15498.
- [58] M. Tsang, D. Cheng, Y. Liu, Detecting statistical interactions from neural network weights, arXiv preprint arXiv:1705.04977 (2017).